INL/RPT-24-81097-Rev000

Laser Shock Modeling Archival Discussion

April 2024

Robert E. Spears

James A. Smith

Bradley C. Benefield

Idaho National Laboratory

INL is a U.S. Department of Energy National Laboratory
operated by Battelle Energy Alliance, LLC

INL/XXX-XX-XXXXX
Revision 0

Laser Shock Modeling Archival Discussion

Robert E. Spears

James A. Smith

Bradley C. Benefield

April 2024

Idaho National Laboratory
Office of Material Management and Minimization
Idaho Falls, Idaho 83415

http://www.inl.gov

Prepared for the
U.S. Department of Energy
Office of Nuclear Energy
Under DOE Idaho Operations Office
Contract DE-AC07-05ID14517

Page intentionally left blank

CONTENTS

FIGURES

Page intentionally left blank

ACRONYMS

INL	Idaho National Laboratory
PEEQ	Equivalent Plastic Strain
PEMAG	Plastic Strain Magnitude

Page intentionally left blank

Laser Shock Modeling Archival Discussion

1. PURPOSE/SCOPE/SUMMARY

The purpose of this discussion is to provide archival information related to the Laser Shock finite element modeling effort. As discussed in "Laser Shock System, assessing bond strength in layered materials" (see Appendix A), the Laser Shock System creates a high-amplitude shockwave on the front of a structure (for our purposes, an aluminum 6061-T6 plate) via a high-energy pulsed laser. The shock wave is monitored on the back surface of the structure as a velocity time history. It is a compressive wave as it moves toward the back surface but reflects as a tensile wave. If a bond exists in the structure and the reflected tensile wave exceeds its interface threshold stress, bond rupture occurs. The aim of the Laser Shock effort is to establish (via multiple tests) an ultimate bond strength usable for fuel plate design calculations. In this regard, the finite element modeling effort is the catalyst for mimicking the Laser Shock tests and providing bond damage information useful for fuel plate design calculations.

The test velocity time history data used for this discussion cover three different Laser Shock intensities, each with five velocity time histories. The test plate is a 1.170-mm-thick aluminum 6061-T6 plate. The scope of this discussion is to outline the finite element model that worked best when trying to model these tests. The finite element models were run in Abaqus 2021.HF6 (2021). The purpose of the finite element model was to accurately model the Laser Shock process so that bond damage can be accurately predicted as a function of Laser Shock intensity, regardless of where the bond is in the plate.

Based on the finite element model results, Abaqus 2021.HF6 appears capable of accurately modeling the Laser Shock process. However, additional calibration is needed in several areas to significantly improve the quality of the results. The most obvious of these areas are the elastic/plastic material property definition, the plastic equivalent strain at failure vs. triaxiality definition (i.e., the ratio of hydrostatic stress to von Mises stress), and the loading application definition. Data estimated based on experiments and the literature were included in the finite element models. (Note that an effort is currently underway at Idaho National Laboratory [INL] to better define, for aluminum 6061-T6, plastic equivalent strain at failure vs. triaxiality.) However, even with the use of estimated input data, the finite element model predicts damage trends that agree well with the actual test results. Consequently, this finite element approach shows promise for converting Laser Shock test data into ultimate (pseudo-static) bond strength data usable for fuel plate design calculations.

2. MATERIAL PROPERTIES

The material properties referred to in this discussion pertain to aluminum 6061-T6. The elastic properties were taken from Table TM-2 of ASME BPVC.II.D.C (2023) (for the modulus of elasticity), and Table PRD of ASME BPVC.II.D.C (2023) (for the Poisson's ratio and density).

Regarding the units selected for the finite element model runs, the important considerations were that the velocity time history be in units of m/s, and that the whole evaluation cover a very short duration of time (namely, the time required for a sound wave to pass through and return through the plate a little over four times). Given these parameters, the units shown in Figure 1 were selected.

mass - μgm

Time - μs

Length - μm

Velocity - $\frac{\mu m}{\mu s} = 1 \frac{m}{s}$

Acceleration - $\frac{\mu m}{\mu s^2}$

Force - $\mu gm \cdot \frac{\mu m}{\mu s^2} = 1 \cdot mN$

Stress - $\frac{\mu gm}{\mu m \cdot \mu s^2} = 1 \cdot GPa$

Density - $\frac{\mu gm}{\mu m^3}$

Figure 1. Definition of units used in this paper.

Based on the above units, the material properties listed in Figure 2 can be defined.

$E_0 := 10.0 \cdot 10^6 \, psi$ Modulus of elasticity

$E_0 = 68.948 \cdot \frac{\mu gm}{\mu m \cdot \mu s^2}$

$\nu_0 := 0.33$ Poisson's ratio

$\rho_0 := 0.098 \cdot \frac{lb}{in^3}$ Density

$\rho_0 = 2.713 \times 10^{-6} \cdot \frac{\mu gm}{\mu m^3}$

Figure 2. Material properties for aluminum 6061-T6.

Below are some additional elastic properties that are either directly defined or can be backed out of equations given in Smith et al. (2016) and Abaqus 2021.HF6, Theory, Elements, Infinite elements, Solid Infinite Elements.

$$G_o := \frac{E_o}{2\cdot(1+\nu_o)}$$ Shear modulus

$$G_o = 25.92\cdot\frac{\mu gm}{\mu m\cdot\mu s^2} \qquad G_o = 25.92\cdot GPa$$

$$K_o := \frac{E_o}{3\cdot(1-2\cdot\nu_o)}$$ Bulk modulus

$$K_o = 67.596\cdot\frac{\mu gm}{\mu m\cdot\mu s^2} \qquad K_o = 67.596\cdot GPa$$

$$E_p := \frac{E_o\cdot(1-\nu_o)}{(1+\nu_o)\cdot(1-2\cdot\nu_o)}$$ Tension/compression stiffness

$$E_p = 102.156\cdot\frac{\mu gm}{\mu m\cdot\mu s^2} \qquad E_p = 102.156\cdot GPa$$

$$v_s := \sqrt{\frac{G_o}{\rho_o}} \qquad v_s = 3091.2\,\frac{m}{s}$$ Shear wave velocity

$$v_p := \sqrt{\frac{E_p}{\rho_o}} \qquad v_p = 6136.7\,\frac{m}{s}$$ Tension/compression wave velocity

$$\sqrt{G_o\cdot\rho_o} = 0.008385\cdot\frac{\mu gm}{\mu m^2\cdot\mu s}$$ Shear nonreflective constant

$$\sqrt{E_p\cdot\rho_o} = 0.016647\cdot\frac{\mu gm}{\mu m^2\cdot\mu s}$$ Tension/compression nonreflective constant

Figure 3.Structural and acoustic properties for aluminum 6061-T6.

Regarding material plasticity, several considerations must be made. Figure 4, Figure 5, and Figure 6 in this report provide data taken from Figure 3, Figure 6, and Figure 9, respectively, in Christman et al. (1971). Regarding Figure 4, Christman et al. (1971) stated that the strain rate sensitivity was "very low at 20°C." The strain rates considered in Christman et al. (1971) are 0.005/sec to 1000/sec, and the Laser Shock test strain rates are closer to $5\bullet10^5$/sec. However, because this is the best available information on this topic, the finite element model covered in the present discussion does not consider strain rate effects. With data that are more appropriate for the Laser Shock tests that are at significantly higher strain rates, strain rate effects may need to be included in the model. Note that a portion of the strain-rate-induced effects are inertial and that these are inherently compensated for in the dynamic finite element model.

Figure 5 provides a range of true stress vs. true strain curves tested in Christman et al. (1971). Figure 6 provides the cyclic behavior tested in Christman et al. (1971). Figure 7 shows the true stress vs. true strain curve used for the discussed model (in units consistent with Figure 5). Figure 8 shows the cyclic loading used for the discussed model (in units consistent with Figure 6). The curve shown in Figure 7 employs a constitutive model definition that provides kinematic hardening (*PLASTIC, HARDENING=COMBINED, DATA TYPE=STABILIZED), follows the shape of a Johnson-Cook constitutive model (Johnson et al. 1983) (with tabular data), and proves reasonable when compared to Figure 5. Smith et al. (2016) also previously used the Johnson-Cook constitutive model. The solver used for this discussion is Abaqus 2021.HF6, which, despite having the Johnson-Cook constitutive model, does not support a kinematic hardening solution. Scoping models indicate that direct usage of the Johnson-Cook constitutive model produces a better initial velocity time history peak, thus tending to indicate that it addresses the compressive wave more accurately. It is also important to note that the Johnson-Cook constitutive model offers features (e.g., the ability to capture thermal responses) that may have a significant impact on material properties. For the reflected wave, such as that reflected in the cyclic loading behavior (Figure 6), the reversed yield stress should occur at a significantly reduced amplitude. A kinematic hardening solution is important for accurately capturing this behavior. Considering that the reflected wave produces the tensile loading that is of greatest concern, and that the kinematic hardening solution is important for accurately modeling stresses, the kinematic solution was selected for inclusion in this discussion. The defined constitutive model generates a reasonable estimate that fosters sensible solutions.

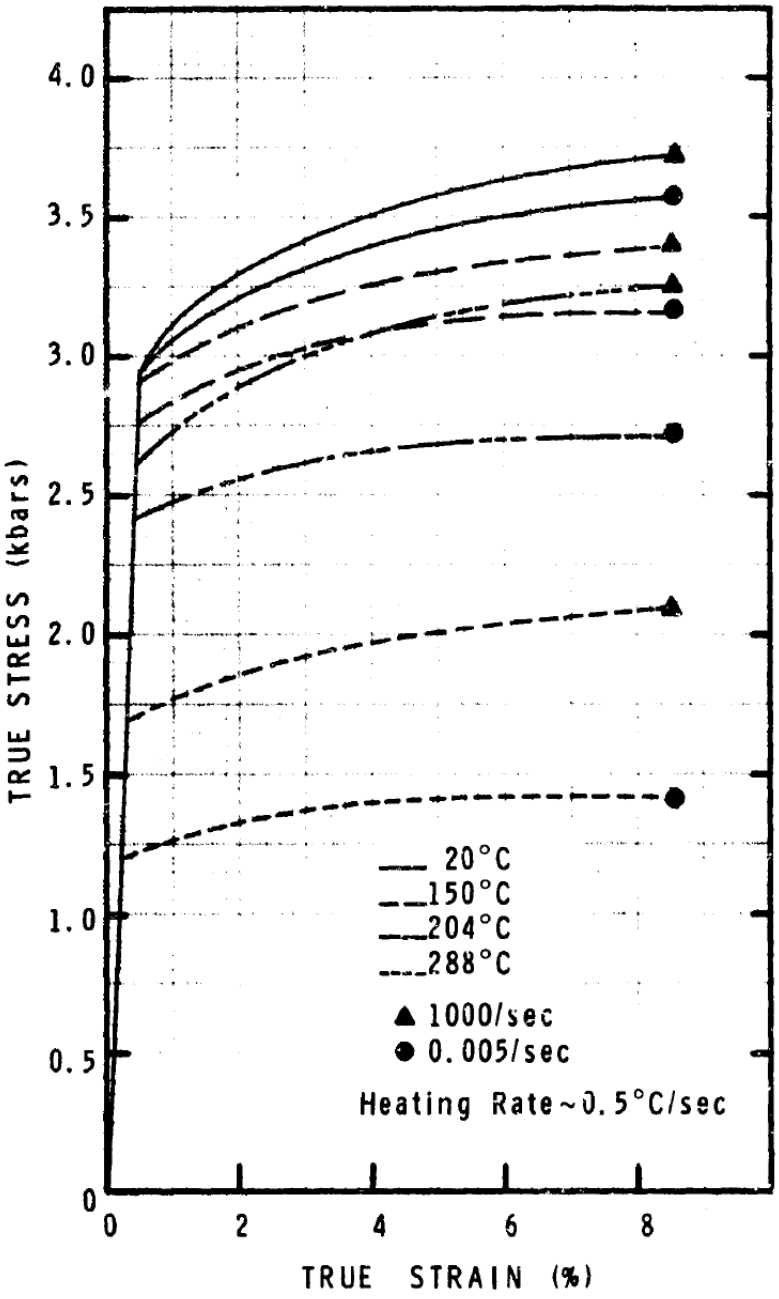

Figure 4. True strain rate tests from Figure 3 in Christman et al. (1971) for aluminum 6061.

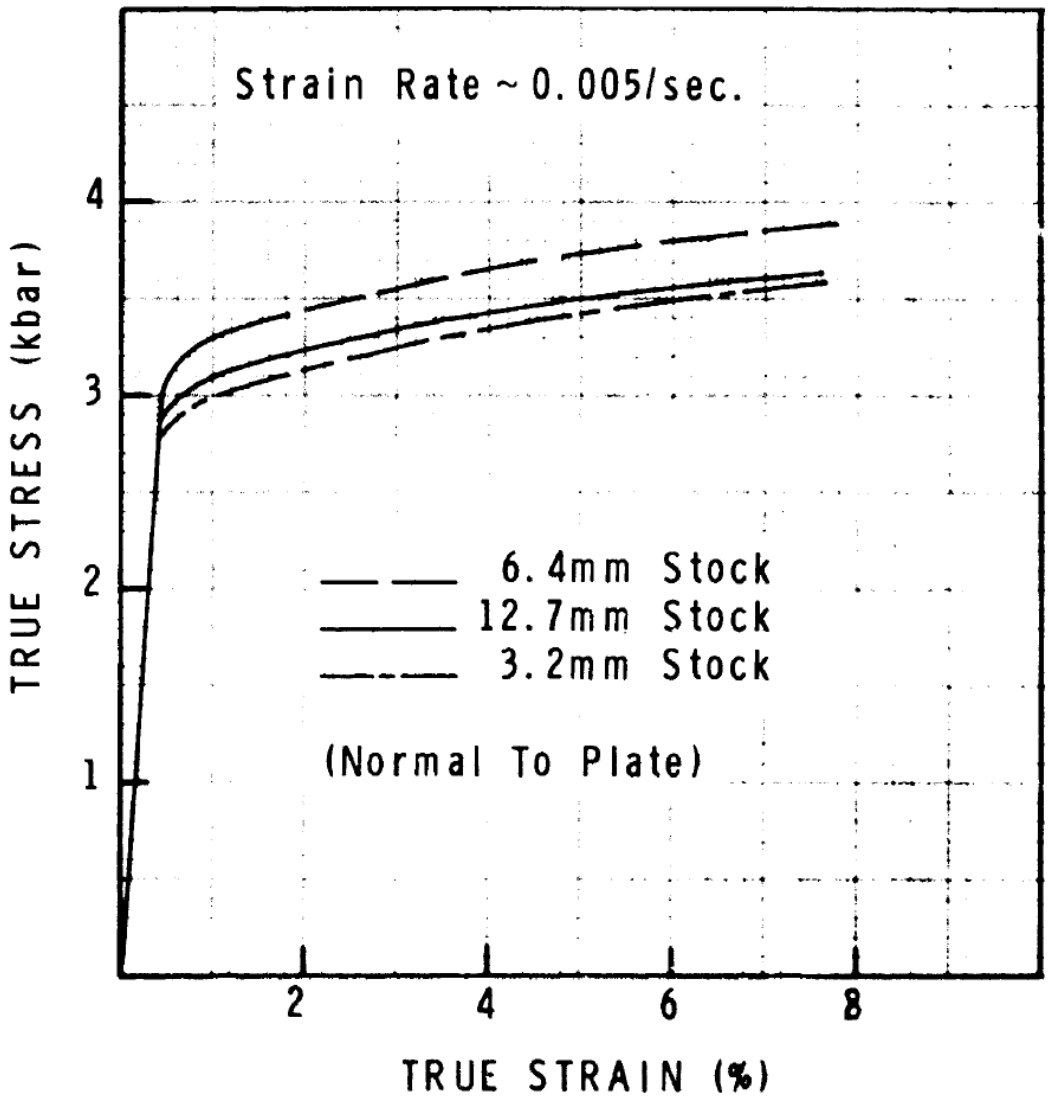

Figure 5. True stress vs. true strain tests material effects in 6061-T6 from Christman et al. (1971).

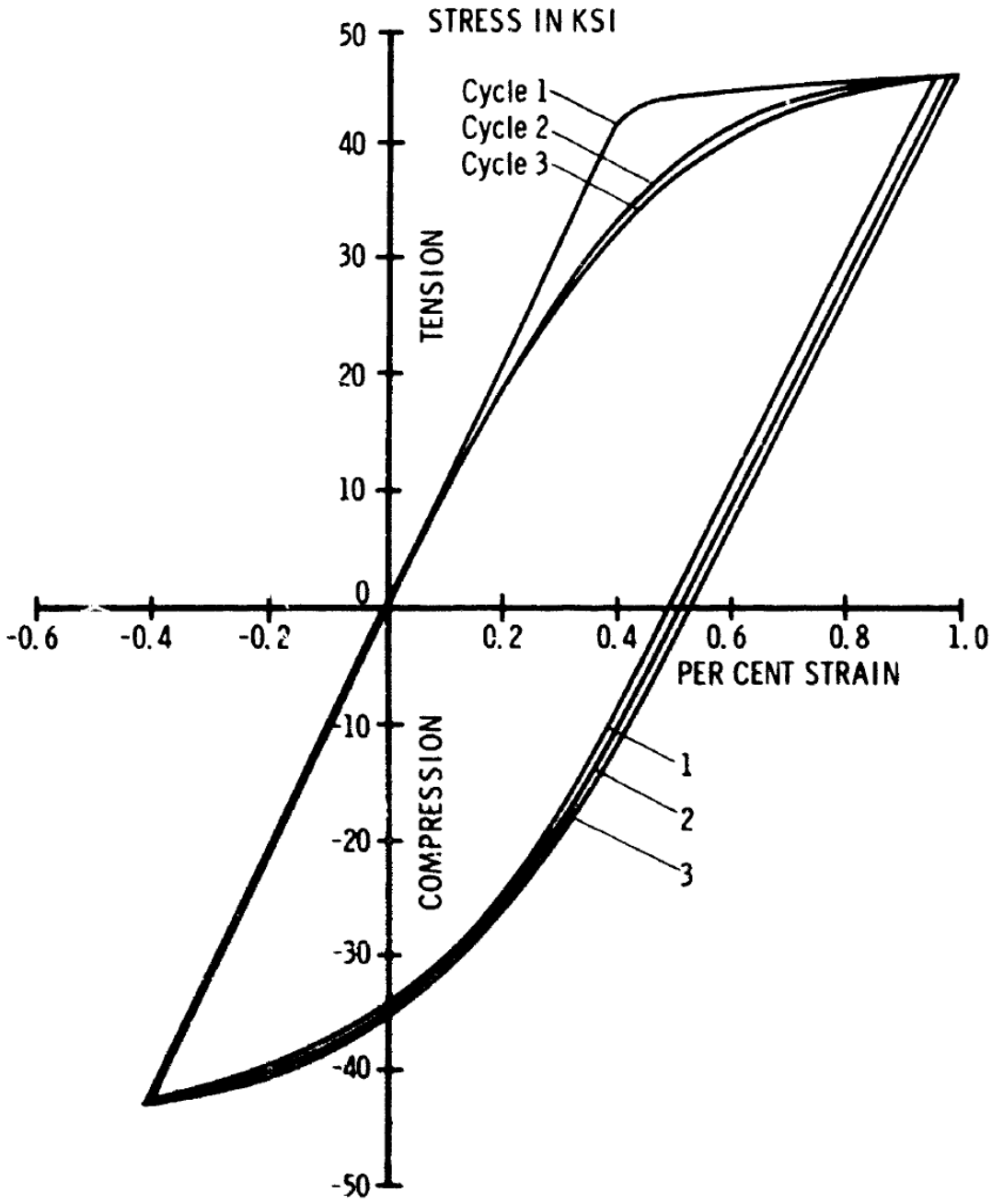

Figure 6. Cyclic loading tests in 6061-T6 from Christman et al. (1971).

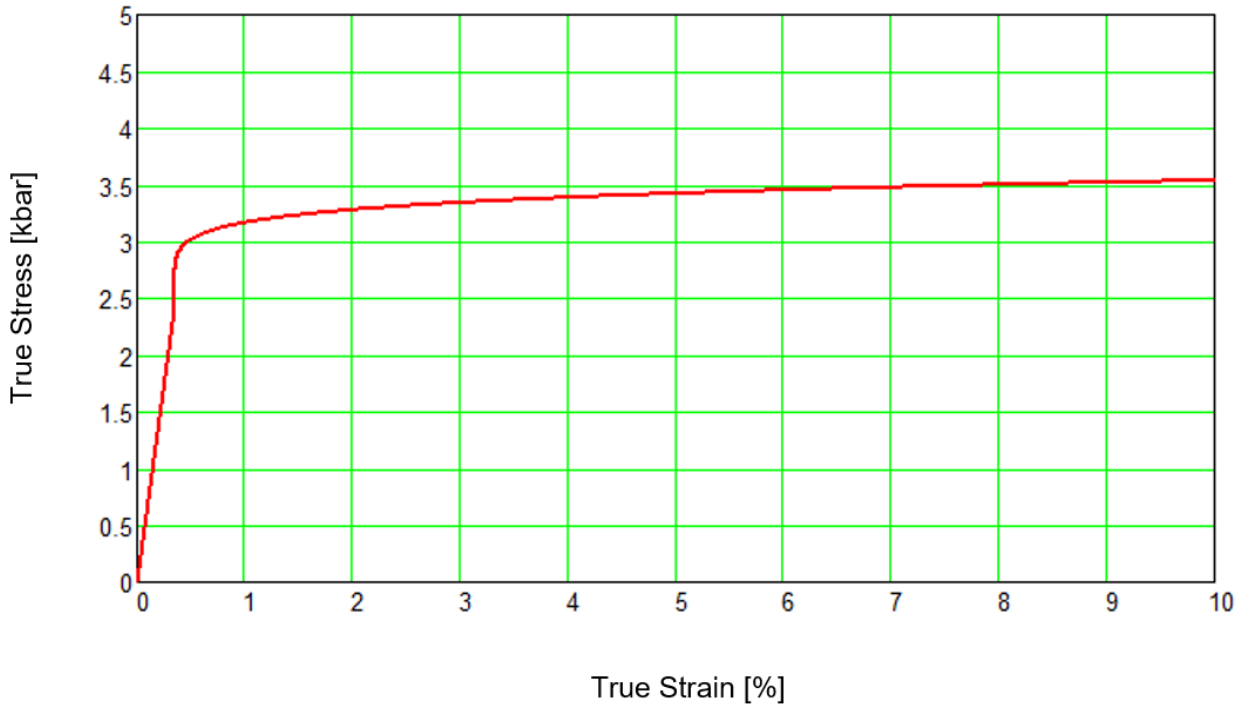

Figure 7. True stress vs. true strain for the discussed model.

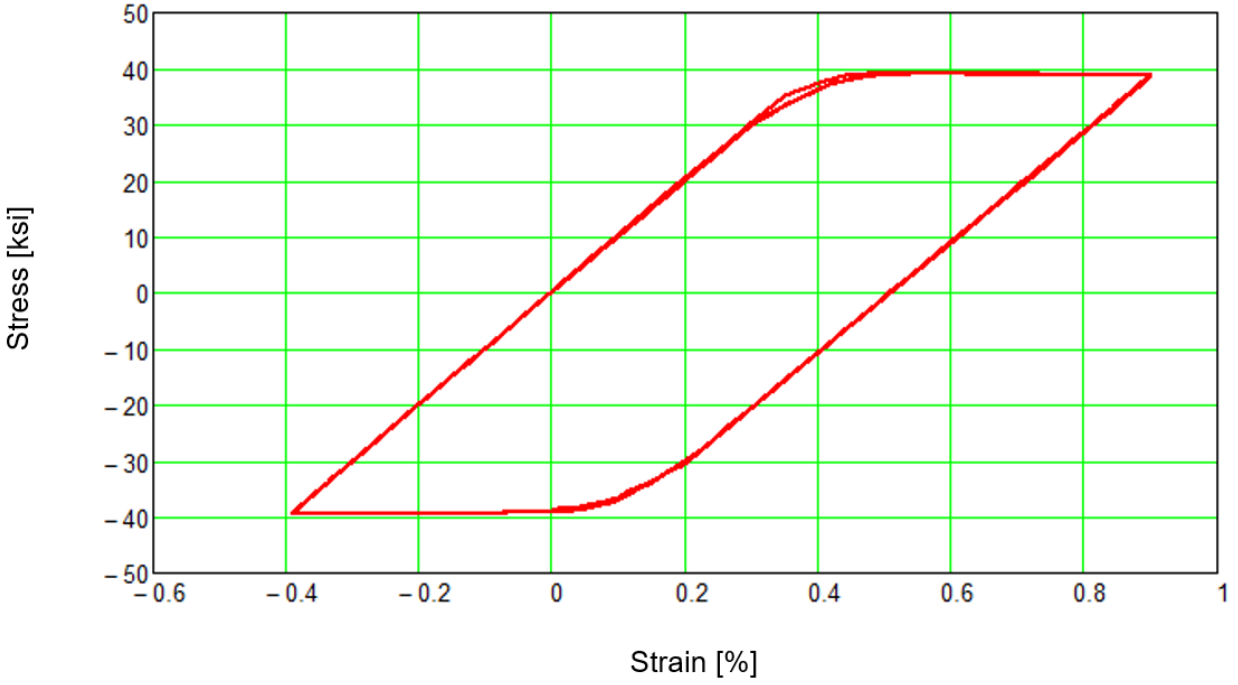

Figure 8. Cyclic loading for the discussed model.

3. FINITE ELEMENT MODELS

The data that were input into the finite element model were believed to contain some inaccuracies and those parameters were adjusted to better match the time history of the surface velocity caused by the propagating shock wave. Five Laser Shock tests were performed at each of the three Laser Shock intensities. Each test was performed at a unique location in the sample, meaning that each was performed on undamaged material.

Section 3.2 describes the finite element mesh used for making comparisons in these tests. The finite element meshes used to collect additional information are discussed in Section 3.2.

3.1. Finite Element Mesh Used for Comparison with the Five Actual Tests

All the finite element model runs whose results were compared against the test data were performed using the parameters shown in Figure 9 and the same mesh (see Figure 10 through Figure 12). The mesh was generated with 459,000 axisymmetric solid elements (*ELEMENT, TYPE=CAX4R)—appropriate for Abaqus 2021.HF6's Abaqus/Explicit solver. The mesh density was defined so as to provide an accuracy equivalent to that of the velocity time history for the actual tests. Velocity time histories are comprised of discrete data points measured at a constant time step. Knowing the time step means that the Nyquist frequency can be established. In turn, knowing the Nyquist frequency and speed of sound in the plate enables establishment of a maximum element length that causes there to be 10 elements per wavelength at the Nyquist frequency. (For numerical analysis, 10 elements per wavelength is normally considered sufficient to produce accurate results).

$\Delta t = 0.002381\ \mu s$ Velocity time history time step

$f_{Nyu} := \frac{1}{2 \cdot \Delta t \cdot \mu s} = 2.100 \times 10^8 \frac{1}{s}$ Nyquist frequency (with units)

$v_p = 6136.7 \frac{m}{s}$ Compression wave velocity

$l_{min} := \frac{v_p}{10 \cdot f_{Nyu}} = 2.922 \cdot \mu m$ Maximum element length to achieve 10 elements per wavelength at the Nyquist frequency

Figure 9. Input parameters into the Finite element model that are sufficient to produce accurate results.

The meshed element length in the direction of the compression/tension wave (y-direction) was 2.6 µm, leading to there being more than 10 elements per wavelength at the Nyquist frequency. The x-direction element length was 4.9 µm, which is perpendicular to the primary direction of motion. However, wave motion in the x-direction is generated from energy propagating radially outward from the Laser Shock input location. This mesh density is considered reasonable for capturing the radial wave propagation.

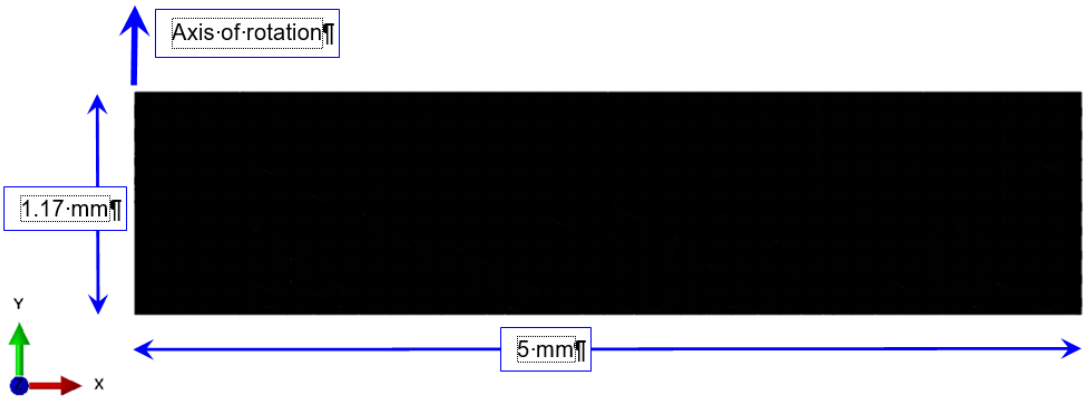

Figure 10. Full mesh, appearing solid black due to the fine mesh borders.

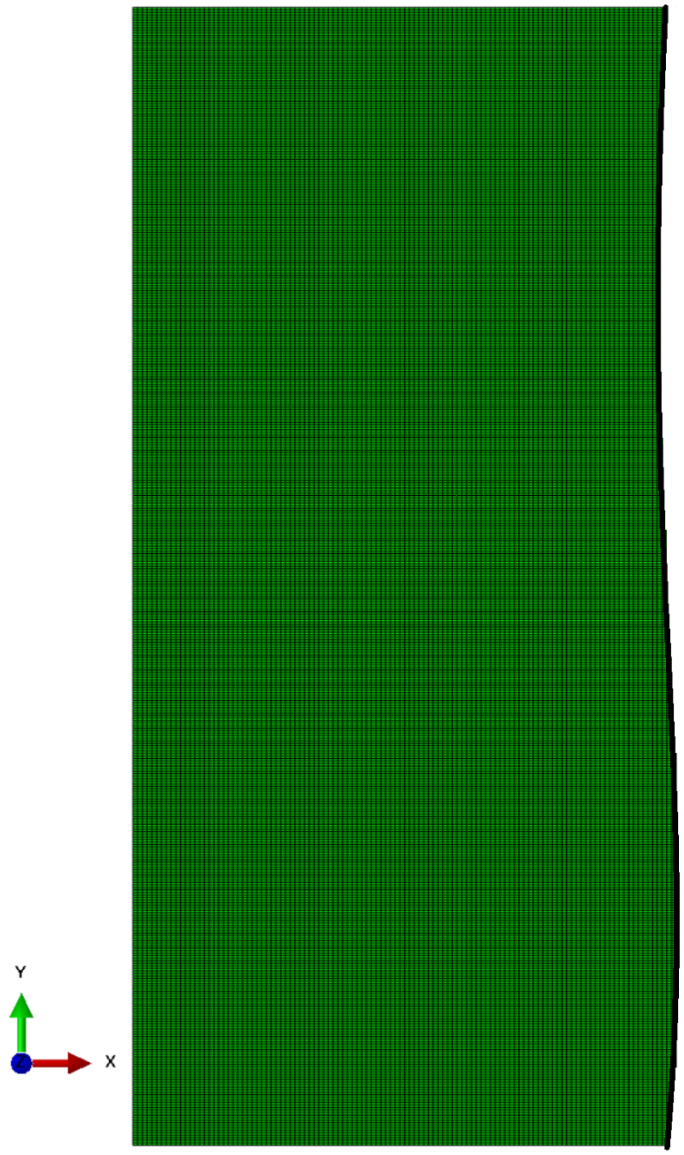

Figure 11. Zoomed-in and cut-away view of the model, near the axis of symmetry.

Figure 12 shows the boundary conditions that remained consistent for all model runs (see Section 4 for the loading definitions). It also shows where the Laser Shock loads were applied, along with the measured velocity time histories. For the boundary conditions, the model was not restrained from translational motion at any location. Instead, the motion was met with resistance from inertia. The positive x-face had nonreflective boundary conditions applied, and these consisted of restraints to prevent rotation, along with dashpots tuned so as to be nonreflective to translational waves. The nonreflective boundary conditions enabled waves to pass out of the model rather than being reflected back into it.

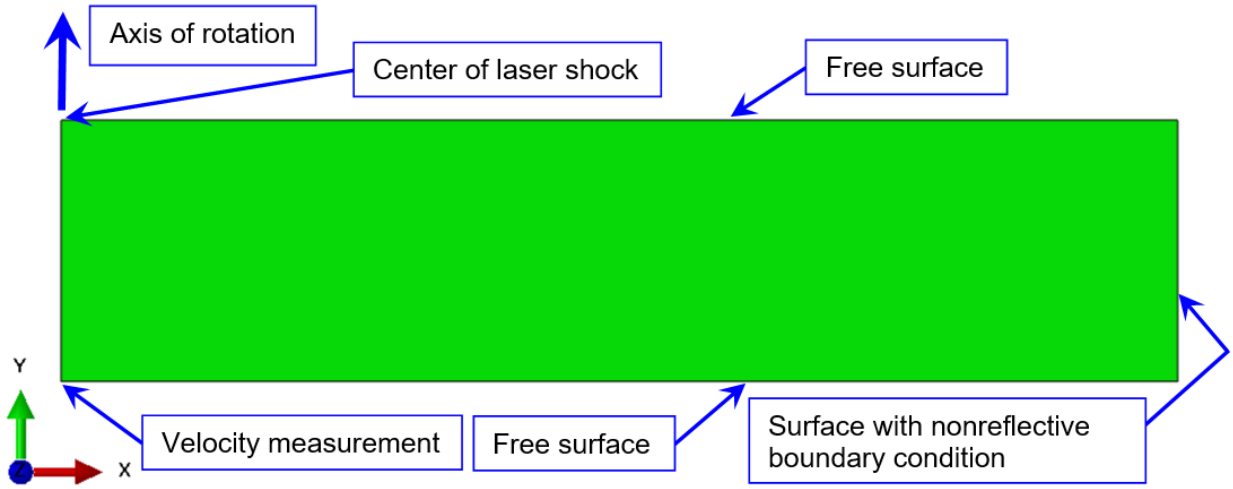

Figure 12. Boundary conditions that remained consistent for all model runs.

The mesh and boundary conditions described in this section appear capable of generating accurate results. The initially explored meshes were performed with solid brick elements, but the axisymmetric approach is both appropriate and much more efficient. After initiating the axisymmetric approach, model sensitivity to x-direction size was not explored. This may be an area in which the model runs can be further calibrated.

3.2. Finite Element Meshes Used for Collecting Additional Information

The finite element meshes used for collecting additional information differ from the model described in Section 3.1 only in terms of y-direction thickness. The model in Section 3.1 is 1.17 mm thick in the y-direction. For this section, three more model thicknesses were considered: 1.110, 1.235, and 1.300 mm. Note that for the selected thicknesses, there are still 10 elements per wavelength at the Nyquist frequency.

4. MODEL LOADING

For the model runs referenced in this discussion, the model output seemed very sensitive to the applied loading. Figure 13 and Figure 14 show the loading used for these model runs. These loading definitions are reasonable—based on the available information—and provide the best results out of all the options that have been tried. Figure 13 shows the Gaussian distribution of the distributed load. The plot shows a radial distribution with values ranging from 0 to 1. These are scale factor values that are multiplied by the time history in Figure 14 to generate a load distribution over time.

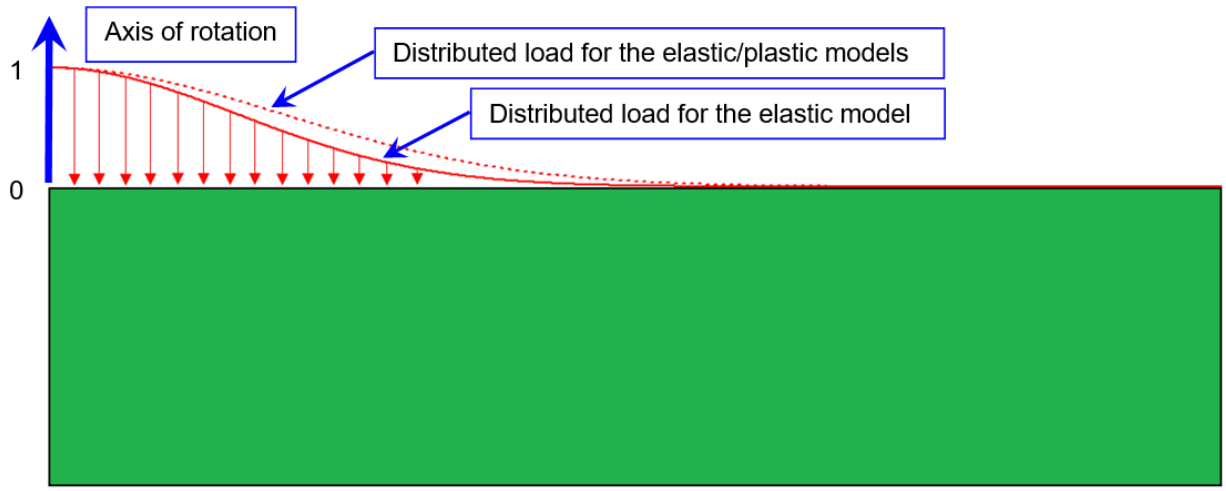

Figure 13. Gaussian distribution, distributed load.

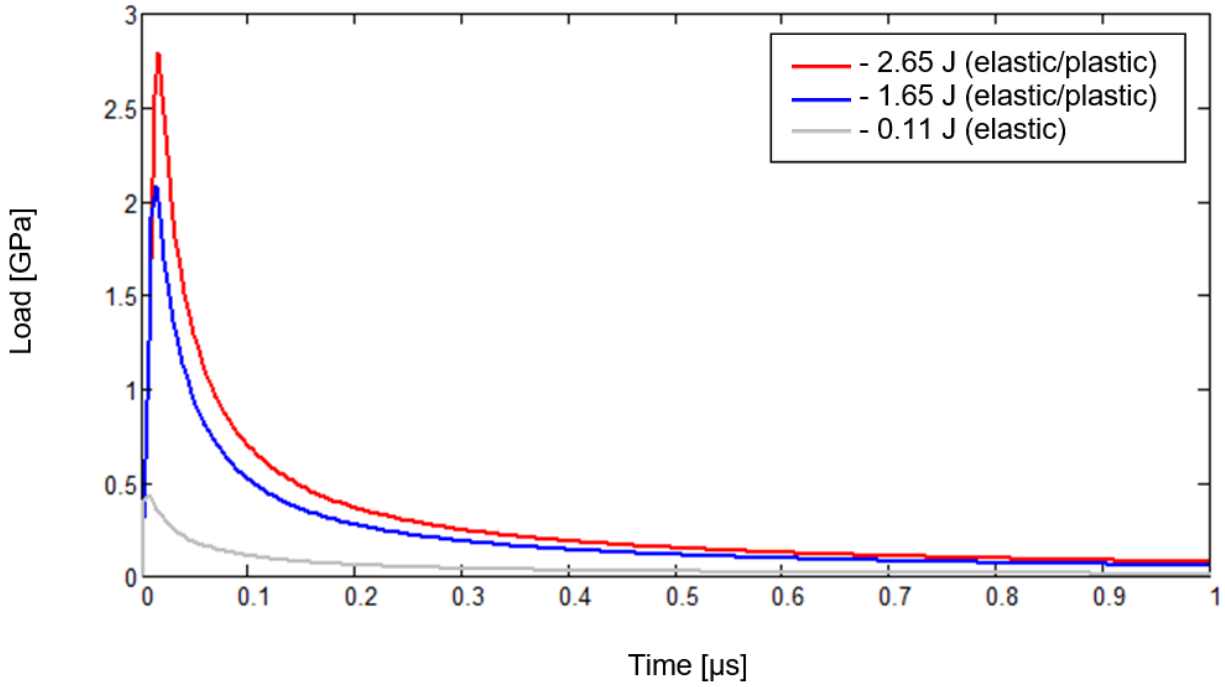

Figure 14. Load time histories.

Many load distributions and time history shapes have been explored. The output velocity time histories seemed very sensitive to these aspects of the models. The Gaussian shape was employed due to previous INL analysts having used it. (Note that the elastic/plastic loading covers a wider radius than the elastic-only loading, enabling the larger "burn" radius to be observed after the tests have been run.) This is not necessarily the correct shape; in fact, it may even vary as a function of time. However, Abaqus 2021.HF6 can handle any variation in loading shape.

The load time history shape is based on two considerations. First, the initial rise is based on the initial rise in the velocity time history. At any given moment in time, the velocity divided by the speed of sound is the strain, and the strain multiplied by the stiffness is the stress. Consequently, the velocity time history is strongly related to the stress time history. Thus, the initial (elastic) rise in the velocity time history should mimic the load time history applied to the opposite surface of the plate. In each curve shown in Figure 14, the increase to peak loading mimics the slope of the velocity time history for each of the tests.

Second, the reduction in the load time history is based on plots taken from slides 6 and 7a of a presentation by Ocaña et al. (2018). The reduction in the load time history in these plots can be approximated using a function defined by 1 divided by a linear function of time. Consequently, this function is used for each curve in Figure 14.

The loading appears to be very important for producing accurate finite element model results. Fabbro et al. (1990) provide an approach to optimizing the basic load time history. Making the quartz gauges small enough to fit multiple gauges within the Laser Shock irradiated location to obtain a load distribution that may foster a more ideal load calibration.

5. MODEL RESULTS

Model results are provided in Section 5.1 through Section 5.3. Section 5.1 provides the primary results for comparison against the actual Laser Shock tests. Section 5.2 gives an example of how the finite element results can be processed to establish pseudo-static bond failure data. Section 5.3 provides additional information on model runs that consider model geometries without employing any actual test data.

5.1. Result Comparison Between the Finite Element Model and the Five Actual Tests

Figure 15 compares the results against the actual test data. Figure 16 through Figure 19 were generated to support converting the finite element model results into something useful to fuel plate analysts.

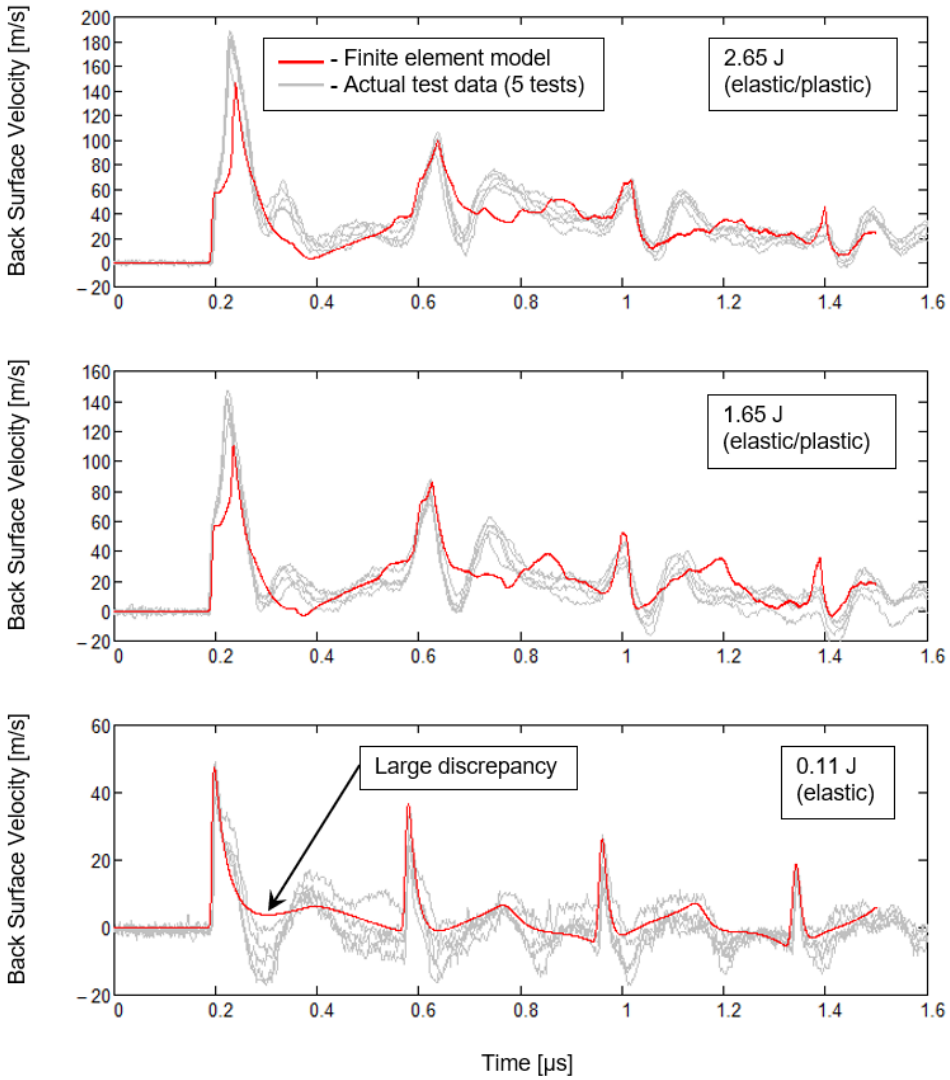

Figure 15. Comparison of the finite element model results against the actual test data.

Per Figure 15, the elastic finite element results are the most accurate of the three models in terms of evaluating the 0.11 J (elastic) results. The elastic finite element model results are mostly within the scatter of the test results, the reflections occur at the correct times, and the amplitude reduction is approximately correct. The largest discrepancy between the elastic test data and the finite element model data likely stems from inaccurate load definition. As noted in Section 4, the loading appears to be very important for producing accurate finite element model results. It is recommended that further load definition calibration be established based on actual tests in which the pressure applied to the sample is directly monitored (though some improvement may be realized by modifying the velocity output by incorporating further applied load iterations in the finite element model).

Per the 1.65 J and 2.65 J (elastic/plastic) results in Figure 15, the elastic/plastic finite element model is sufficiently accurate to be useful. The reflections occur on time, and the amplitude reduction is on par with the experimental data. Furthermore, for a notable portion of the timeframe, the results are within the scatter of the test results. However, discrepancies are seen that are similar yet more persistent than in the elastic model, and the initial peak amplitude is not achieved. These discrepancies likely stem from inaccurate load definition (as in the case of the elastic finite element model results) and inaccurate material properties. As noted in Section 2 and Section 4, the elastic/plastic material properties and loading definition appear to be very important for producing accurate finite element model results. It is recommended that further load definition calibration be established based on actual tests (though again, some improvement may be realized by iteratively modifying the finite element model to improve the velocity output).

Figure 16 through Figure 18 show the tensile wave occurring at 0.3 µs for the respective models listed in Figure 15. For all three plots, the compressive wave has reflected off the bottom surface and then turned into a tensile wave. The plots represent the first reflection, with the tensile wave now moving upward.

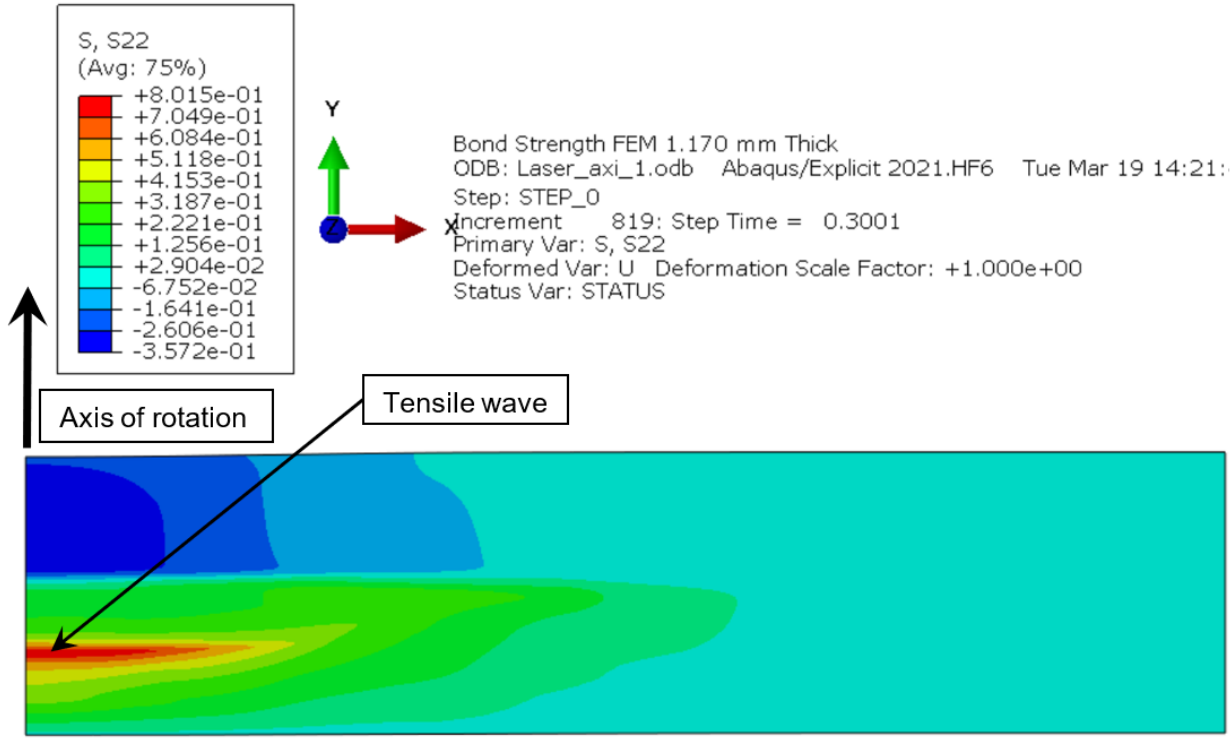

Figure 16. Tensile wave at 0.3 µs for 2.65 J (elastic/plastic).

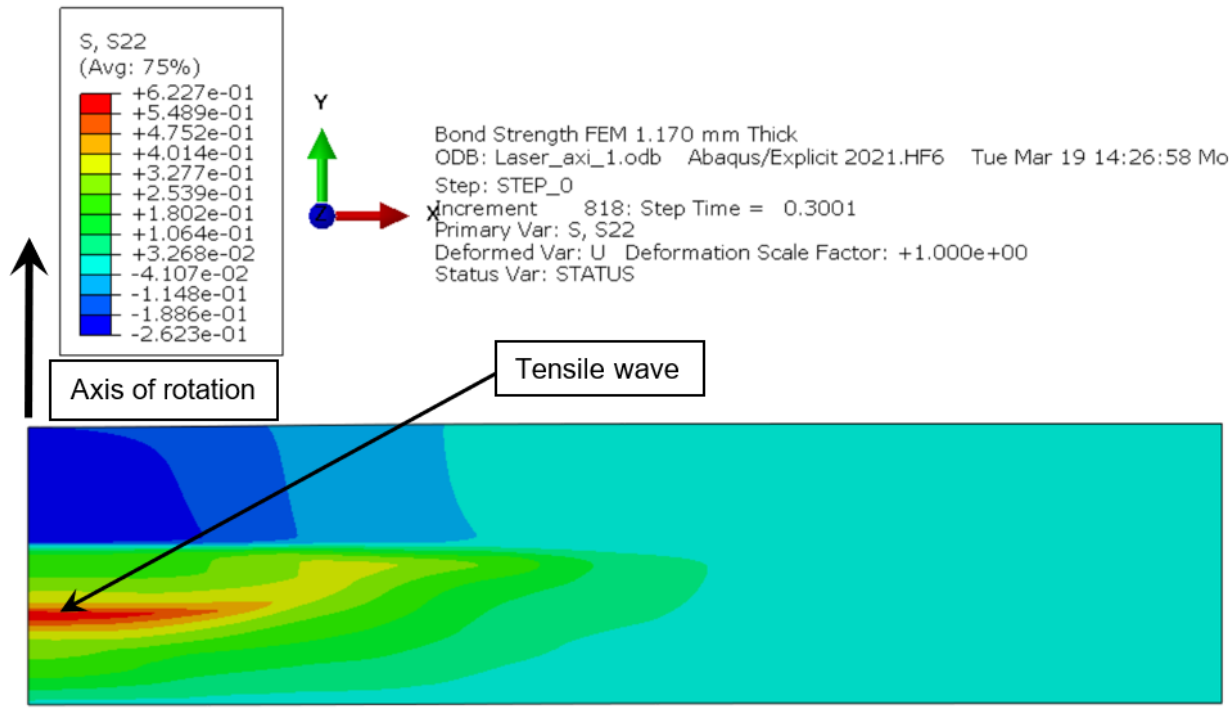

Figure 17. Tensile wave at 0.3 μs for 1.65 J (elastic/plastic).

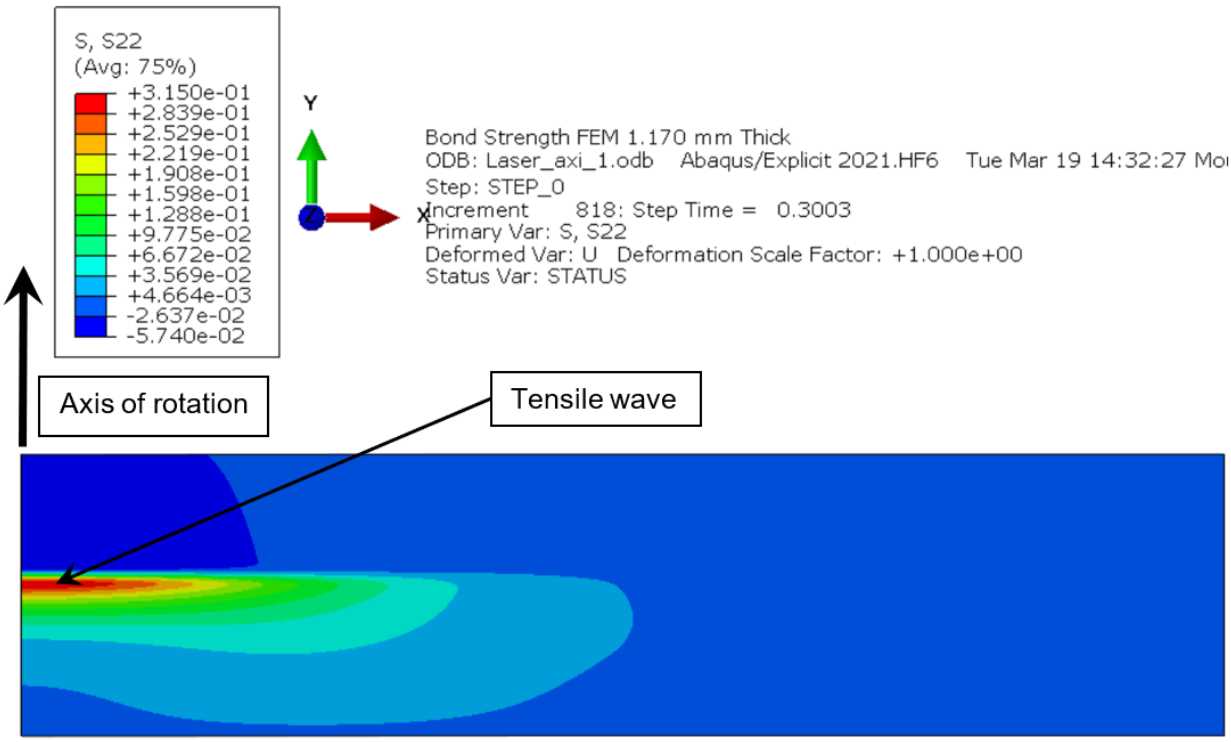

Figure 18. Tensile wave at 0.3 μs for 0.11 J (elastic).

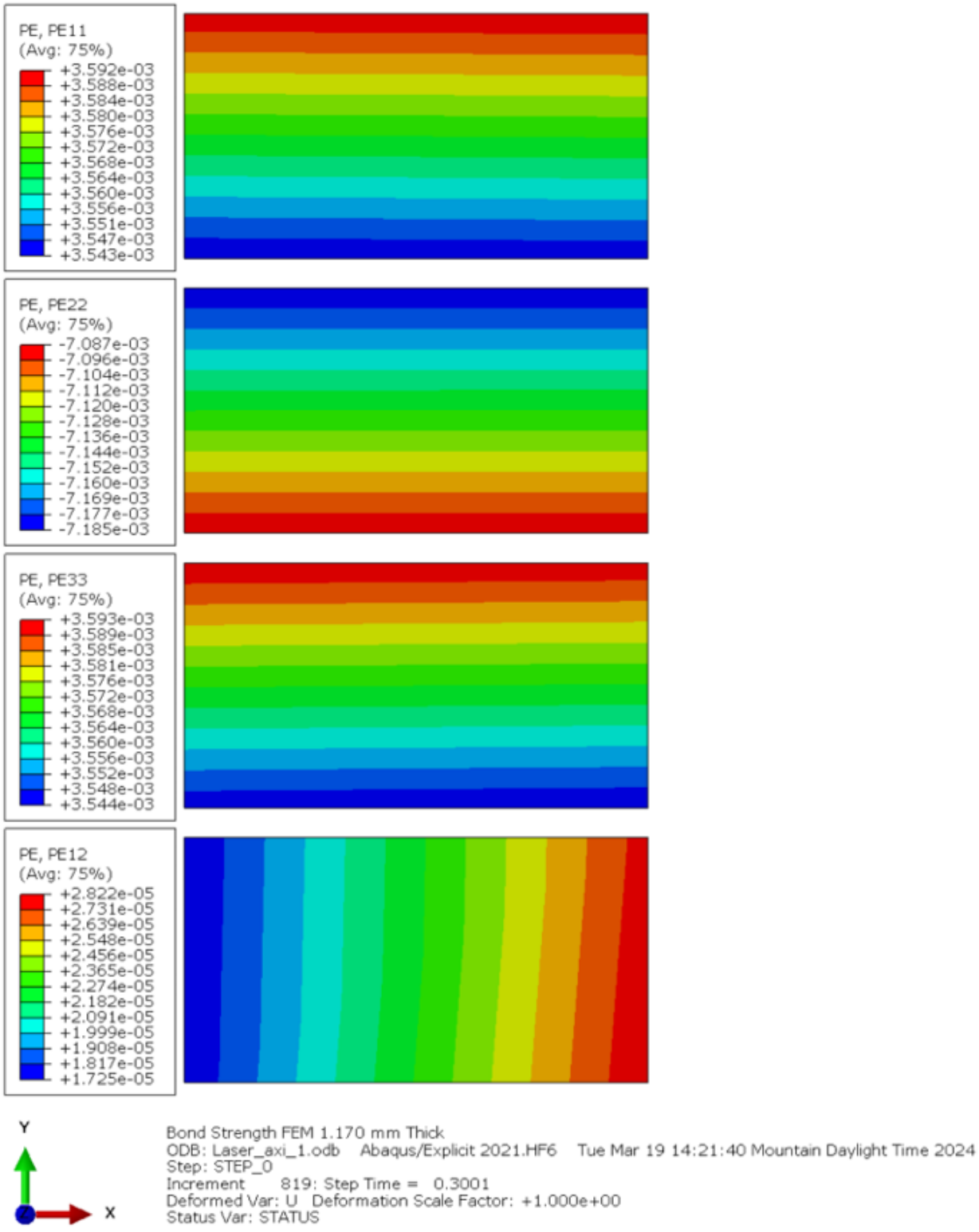

Figure 19. Plastic strains in an element, with the peak tensile stress from Figure 16.

In Figure 18, there are no plastic strains, and the stresses represent how a bond would be challenged. In Figure 16 and Figure 17, there are significant plastic strains, and challenging a bond becomes a little more complicated. Figure 19 shows the plastic strains in an element, with the peak tensile stress from Figure 16. As is seen, the results reflect a relatively complex strain state. Assuming that the finite element model is sufficiently accurate to capture the strain state well, the tensile wave is insufficient to reverse the compressive plastic strains. However, damage can be measured as a function of how close the plastic strains are to failure given the stress state (triaxiality).

For aluminum 6061-T6, an effort is currently underway at INL to determine the plastic equivalent strain at failure as a function of triaxiality (i.e., the ratio of hydrostatic stress to von Mises stress). Using triaxiality, a complex strain state can be evaluated to find out how close it is to causing failure (in the base material). With this approach, the following steps can be used to establish the plastic equivalent strain needed to cause bond failure (assuming the bond fails in a similar manner as the base material).

1. Laser Shock tests are employed to establish the energy needed to cause bond failure and finite element modeling is performed to mimic the test by finding the complex strain state and triaxiality at the bond interface.
2. The true strain state and triaxiality can be used to establish how near the base material is to failure by determining the quasistatic failure value.
3. Bond failure plastic equivalent strain can be defined as a percentage of plastic equivalent strain (dynamic) to base material (quasi-static) failure (referred to as the “damage ratio” in Section 5.2).
4. The damage ratio is then mapped onto the tensile pull test (Figure 7) to obtain the bond strength in terms of stress (see Section 5.2.2).

The typical design analysis for a bond is performed with a continuous mesh and a known location of the bond. The base material von Mises stresses and/or plastic equivalent strains are then found at the bond location, as determined per the given design conditions. Ideally, triaxiality would then be used with plastic equivalent strain at the bond, as determined per a percentage of base material failure (damage ratio). The results from Step 4 can be used to establish a safety factor against bond failure for a given component design.

To translate the Laser Shock debond thresholds into design criteria for structural performance, an approximate approach can be used. Step 4 can be used to establish the bond failure plastic equivalent strain (or stress), based on a simple pull test of the base material (triaxiality = 1/3, as shown in Figure 21). The von Mises stresses and/or plastic equivalent strains obtained from performance modeling of the structure can then be compared to the bond failure plastic equivalent strain. This comparison can be used to establish a safety factor against bond failure for the given structural design. The bond strength in terms of true stress is determined by mapping the damage ratio onto the tensile pull test.

5.2. Processing the Results to Establish Pseudo-Static Bond Failure Data

To process the results for establishing pseudo-static bond failure data, the basic logic identified in Section 5.1 needs to be more rigorously defined. In this regard, Section 5.2.1 defines the triaxiality and failure strain for the example referenced in this discussion. Damage ratio (i.e., bond failure to base material failure as a function of plastic equivalent strain) is defined in Section 5.2.2.

For the three test cases, the results of Step 1 (experimental results) and Step 2 (modeled results) from the list of steps given in the previous section are shown in Figure 15.

5.2.1. Triaxiality and Failure Strain

By recognizing that failure strain in a material varies with triaxiality, plastic strains can be evaluated as a function of how close they are to the failure strain. In lieu of final data from INL’s aluminum 6061-T6 triaxiality effort, the quasi-static failure strain as a function of stress triaxiality ratio that is presented in

Fig. 14 in Grytten et al. (2009) is used instead. This figure is approximated, noting that the triaxiality curve was generated for a different aluminum alloy. In Figure 21, the curve was converted to true plastic equivalent strain vs. triaxiality, which is part of Step 3 (determining the quasistatic failure value). The fact that kinematic hardening is used and the strains are being reversed makes Abaqus 2021.HF6, Equivalent Plastic Strain (PEEQ) unsuited for establishing failure strain. PEEQ is cumulative and thus appropriate for isotropic hardening and/or loading that is not reversed. Consequently, Abaqus 2021.HF6, Plastic Strain Magnitude (PEMAG), which is not cumulative, will be used in this discussion (for calculating the plastic equivalent strain). Abaqus 2021.HF6, PEMAG, states:

"For most materials and only proportional loading, PEMAG is equal to PEEQ. It is available only with Abaqus sensitivities."

Because PEMAG is only available for specific applications in Abaqus, the plastic strain components shown in Figure 19 are output and PEMAG is calculated in post-processing. The equation for PEMAG from Abaqus 2021.HF6 produces the following equation using the plastic strain components shown in Figure 19 (where PE11 is normal plastic strain in the 1-direction, PE12 is shear plastic strain in the plane of the elements, PE22 is normal plastic strain in the 2-direction, and PE33 is normal plastic strain in the 3-direction):

$$PEMAG = \sqrt{\frac{2}{3}} \cdot \sqrt{PE11^2 + 2 \cdot PE12^2 + PE22^2 + PE33^2}$$

Figure 20. PEMAG is calculated by geometrically summing all the plastic strain directions. (Note: The shear strains in this equation are tensor strains. When shear strains are output from Abaqus, they are given in engineering strains. Consequently, if PEMAG is calculated using plastic strain output from Abaqus, the shear strains must be divided by 2 before being put into the equation.)

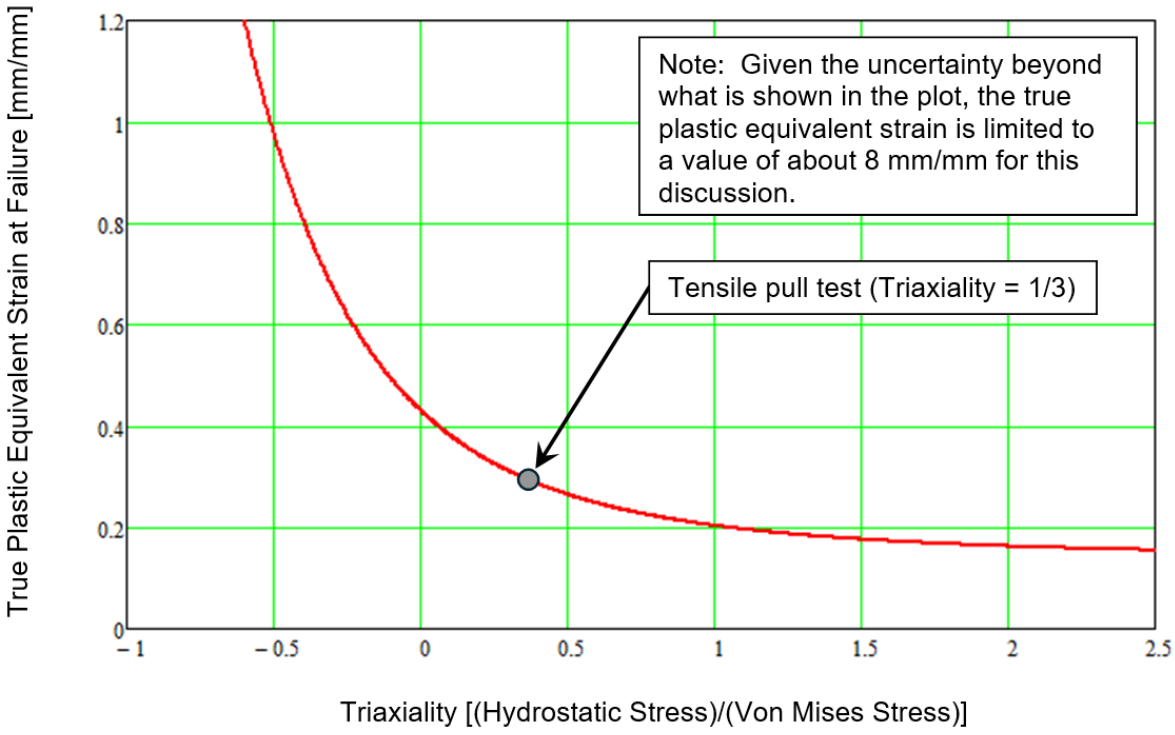

Figure 21. Approximation of true plastic equivalent strain at failure vs. triaxiality. This graph is used for Step 3a (determining the quasistatic failure value).

5.2.2. Damage Ratio

For the purposes of this discussion—considering the definition of true plastic equivalent strain at failure vs. triaxiality—a damage ratio can be defined (Step 4) if a given plastic equivalent strain value is deemed just sufficient to cause bond failure and its triaxiality is also known. Using the triaxiality value along with Figure 21, a plastic equivalent strain value can be found that causes base-material failure. The damage ratio can then be defined as the plastic equivalent strain ratio for bond failure, divided by that for base-material failure. With the known bond failure damage ratio, a similar damage ratio approach can be defined for the plastic equivalent strains from the performance analysis of a fuel plate design. Finally, the two damage ratios can be compared to establish a safety factor against bond failure.

Instead of a case-by-case evaluation based on finite element modeling of differing Laser Shock energies and plate geometries, an interpolation tool can be developed to provide a more generalized evaluation. Laser Shock tests of various intensities would be performed on base material only (i.e., no bond), with a variety of plate geometries. Damage ratio calculations as a function of position through the plate thickness would be performed using the appropriate finite element models, and the results would be stored in a matrix. A lookup table/plot could be generated that provides, for various geometries, the damage ratio as a function of Laser Shock intensity and bond position through the thickness. Then, when a Laser Shock test is performed on a similar plate geometry with a bond interface, the interpolated damage ratio for that bond failure could be quickly determined, leading to a bond strength measurement independent of plate geometry (automating Steps 2–5).

By using the Laser Shock tests and finite element models referenced in this discussion, the damage ratio as a function of thickness ratio can be found (see Figure 22). (Note that the thickness ratio is simply the position in the thickness, divided by the total thickness.) Figure 22 was developed by searching for the maximum damage ratio—over the whole-time history—for elements centered under the Laser Shock location at regular intervals through the thickness.

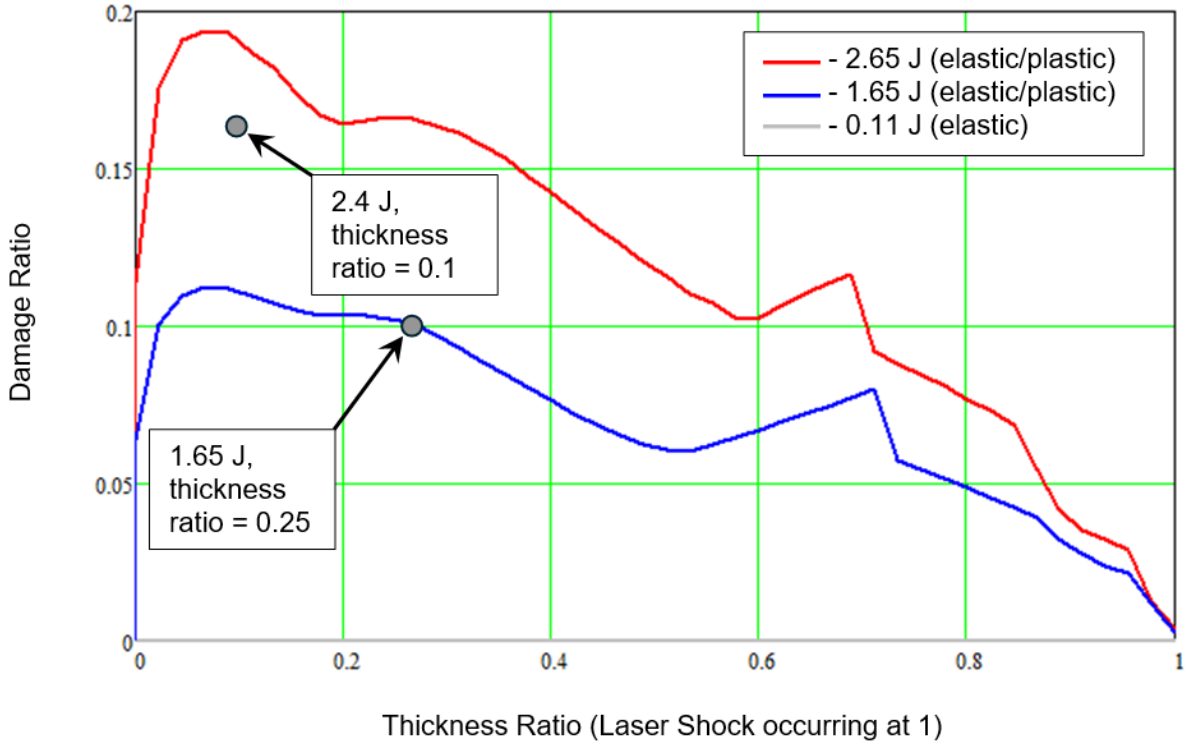

Figure 22. Damage ratio through the thickness (Step 4).

In Figure 22, the damage ratio through the thickness seems to agree well with trends indicated by actual tests to produce bond failure. The trends shown in Figure 22 make it obvious that Laser Shock testing should be performed with the bond located as far as possible from where the Laser Shock is applied (i.e., it should never have a thickness ratio of over 0.5). Using this approach, less energy is necessary to fail a bond, and bond failure is much more sensitive to the Laser Shock intensity.

Per Figure 22, an example could be considered in which a Laser Shock test is performed at 1.65 J with a bond located a quarter of the distance from the side of the plate opposite the Laser Shock interrogation area that has a thickness ratio = 0.25, as shown in Figure 22). If these conditions define a bond strength threshold, the damage ratio from Figure 22 for that bond would be approximately 0.1. In other words, the bond would fail at approximately a tenth the plastic equivalent strain needed to fail the base material.

If instead, the bond strength threshold occurred at an intensity of 1.65–2.65 J, interpolation could be used to estimate the damage ratio. The example point in Figure 22 that corresponds to 2.4 J and a thickness ratio of 0.1 produces a damage ratio of about 0.16, meaning that the bond would fail at approximately 16% of the plastic equivalent strain needed to fail the base material. Through additional testing and finite element modeling, a wide range of damage ratio curves can be addressed.

Figure 23 shows the pull-test true stress vs. true plastic strain. (Note that Figure 23 is similar to Figure 7, except that the elastic strain is removed, leaving only the plastic strain component.) By considering the example bond failure data points from Figure 22, the bond failure can now be identified (see Figure 23) relative to a pull test. For the point (1.65 J, thickness ratio = 0.25) with a damage ratio of about 0.1, bond failure in a pull test should occur at approximately 0.86% (0.1•8.6%) plastic strain, which generates a bond failure stress of approximately 3.20 kbar (Step 5). For the point (2.4 J, thickness ratio = 0.1) with a damage ratio of about 0.16, bond failure should occur in a pull test at approximately 1.38% (0.16•8.6%) plastic strain, which generates a bond failure stress of approximately 3.26 kbar (Step 5).

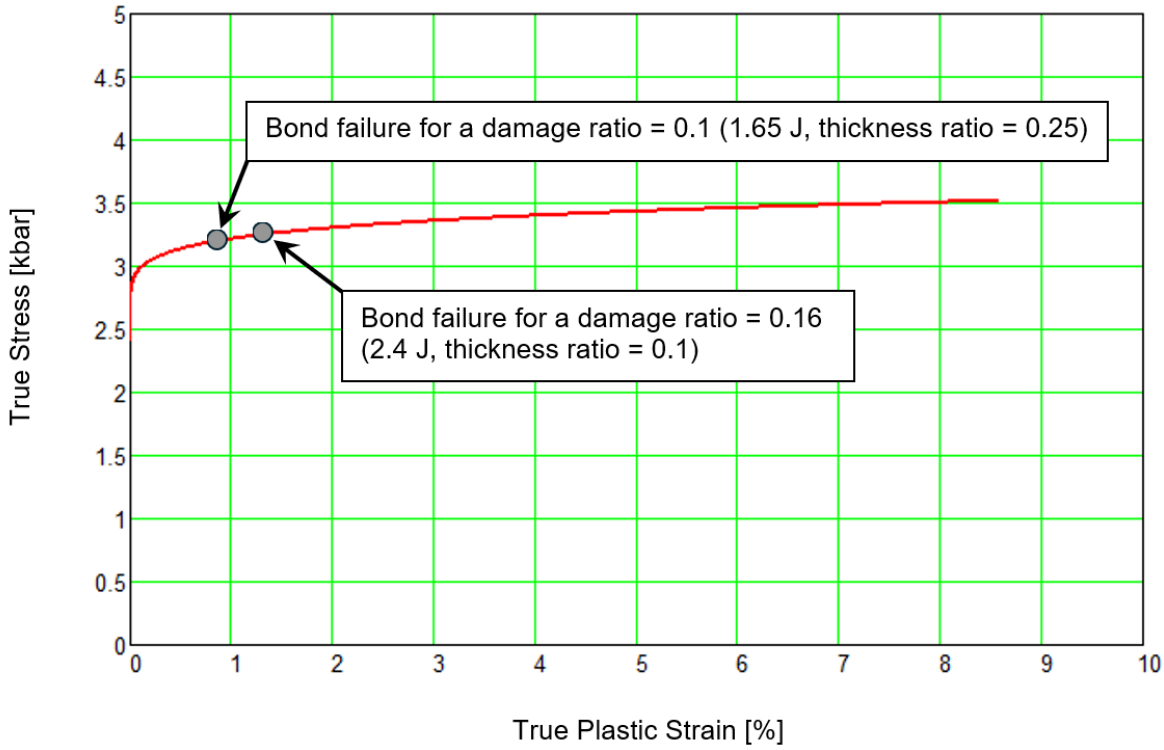

Figure 23. True stress vs. true plastic strain, with bond failure identified (relative to a pull test).

5.3. Additional Results for Collecting Information

To collect information, additional model runs were performed on geometries for which there were no test data. The plate used for the testing was 1.170 mm thick in the y-direction. Additional models were run with 1.110, 1.235, and 1.300 mm thicknesses. In all cases, the mesh contained the same number of elements. The elements were simply scaled in size throughout the thickness. It should be noted that this scaling did not cause there to be fewer than 10 elements per wavelength at the Nyquist frequency.

Figure 24 shows the damage ratio results from all the model runs. The resulting curves are generally predictable and reasonable, though certain anomalies do arise when exceeding a thickness ratio of about 0.6. However, as noted in Section 5.1, a bond undergoing testing should not be at a location whose thickness ratio exceeds 0.5 (i.e., if the thickness ratio is over 0.5, the Laser Shock should be applied to the opposite side of the plate, thereby applying maximum stress to the bond while utilizing the minimum amount of Laser Shock intensity).

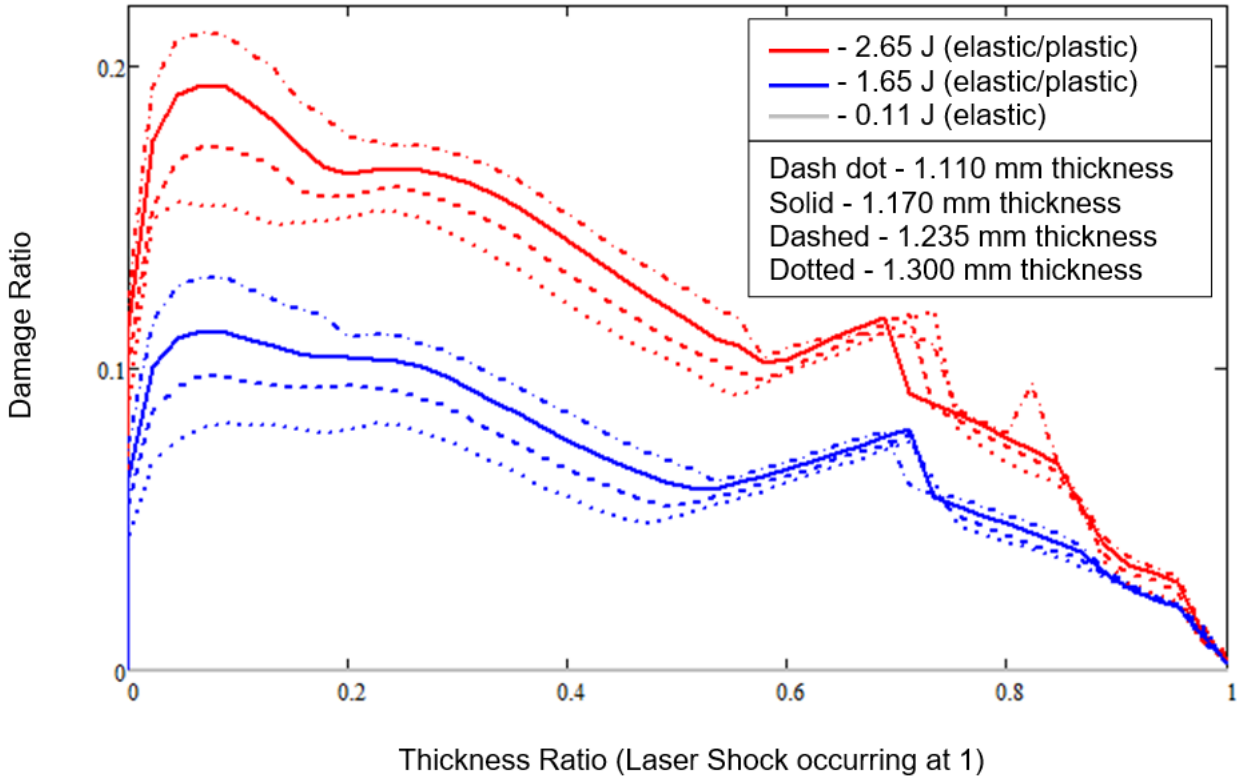

Figure 24. Damage ratio through the thickness, for multiple geometries.

6. CONCLUSIONS/RECOMMENDATIONS

For the purpose of this discussion, a finite element model was generated that provides sensible results. The input data available for calibrating the Laser Shock finite element model include a velocity time history (taken from the opposite surface and centered on where the Laser Shock is applied), a burn mark in the tape (where the Laser Shock is applied, and which can be used to determine the laser spot size), an aluminum plate containing a plastically deformed region (marking the travel path and plastic deformation on both surfaces), and a degree of experience-based bond failure knowledge acquired from previous Laser Shock tests. No material property tests were performed on the tested aluminum plates for calibration purposes, no tests were performed to calibrate how the load was applied, and no actual test time histories were taken from any other locations on the aluminum plate. Furthermore, many papers on similar topics served to provide a degree of guidance, though said guidance was not necessarily specific to this setup. Consequently, many variables had to be adjusted, with sparse knowledge as to what the proper parameters should be.

Per the finite element results, further calibration is needed in three obvious areas: the elastic/plastic material property definition, the plastic equivalent strain at failure vs. triaxiality definition, and the loading application definition. In none of these three areas are sufficiently accurate/applicable data readily available for inclusion in the finite element models. However, even with incomplete calibration, the finite element models predict damage trends that agree well with the actual test results. Consequently, this finite element approach shows promise for converting Laser Shock test data into ultimate (pseudo-static) bond strength data usable for fuel plate design calculations. Furthermore, Abaqus 2021.HF6 proved capable of accurately modeling the Laser Shock tests.

7. EXAMPLE ABBREVIATED ABAQUS INPUT FILE

An example abbreviated input file is given below for the 1.170-mm-thick aluminum plate, with the highest intensity load being input. The top-level input file “Laser_axi_1.inp” is given in its entirety (except for a few cards that were not being used and were disabled by placing two stars in front of them). For efficiency in the included files (ending in “.i”), voluminous data such as node and element data are removed (“…” denotes removed data). By employing this technique and referencing the discussion covered in Section 2 through Section 4, it should be possible to generate a similar complete input file. The other input files differ in terms of nodal position and input load time histories. The input file below is run in Abaqus 2021.HF6’s Abaqus/Explicit solver (see Section 2 for the model units).

Laser_axi_2.inp

```
*HEADING
Bond Strength FEM 1.170 mm Thick
**
** Nodes and Elements
*NODE, NSET=ALL
*INCLUDE, INPUT=z_Nd_axi.i
**
*ELEMENT, TYPE=CAX4R, ELSET=ALL
*INCLUDE, INPUT=z_El_axi.i
**
*INCLUDE, INPUT=z_Nonreflect_axi.i
*INCLUDE, INPUT=z_Material_Section_Kinematic_JoCo2a.i
*INCLUDE, INPUT=z_Sets_axi.i
**
** Load Time History
*INCLUDE, INPUT=z_Load_Time_History_var2.i
**
** Restraints
*INCLUDE, INPUT=z_BC_axi.i
**
** ----------------------------------------------------------------
```

```
**
** STEP: STATIC
**
*STEP, NAME=STEP_0
*DYNAMIC, EXPLICIT
 , 1.5
*BULK VISCOSITY
 0.06, 1.2
**
** Applied Loading
*DLOAD, AMPLITUDE=LOAD_1
*INCLUDE, INPUT=z_DLOAD_G_axi_pl.i
**
*RESTART, WRITE, NUMBER INTERVAL=0, TIME MARKS=NO
**
*OUTPUT, FIELD, TIME INTERVAL=0.0125
*NODE OUTPUT
A, RF, U, V
*ELEMENT OUTPUT, DIRECTIONS=YES
LE, PE, PEEQ, PEMAG, S
*OUTPUT, HISTORY, FREQUENCY=1
*NODE OUTPUT, NSET=OUTPUTND
A2, U2
*NODE OUTPUT, NSET=OUTPUTND
V2,
*ELEMENT OUTPUT, ELSET=OUTPUTEL
S22, MISES, TRIAX, LODE, PE11, PE22, PE33, PE12, PEEQ, PEMAG
*OUTPUT, HISTORY, VARIABLE=PRESELECT, TIME INTERVAL=0.0001
*MONITOR, NODE=10000000, DOF=2
*END STEP
```

z_Nd_axi.i

```
10000000, 0, -1170, 0
10000001, 4.90196078431373, -1170, 0
10000002, 9.80392156862745, -1170, 0
10000003, 14.7058823529412, -1170, 0



10460467, 4985.29411764706, 0, 0
10460468, 4990.19607843137, 0, 0
10460469, 4995.09803921569, 0, 0
10460470, 5000, 0, 0
```

z_El_axi.i

```
10000000, 10000000, 10000001, 10001022, 10001021
10000001, 10000001, 10000002, 10001023, 10001022
10000002, 10000002, 10000003, 10001024, 10001023
10000003, 10000003, 10000004, 10001025, 10001024



10458996, 10459445, 10459446, 10460467, 10460466
10458997, 10459446, 10459447, 10460468, 10460467
10458998, 10459447, 10459448, 10460469, 10460468
10458999, 10459448, 10459449, 10460470, 10460469
```

z_Nonreflect_axi.i

*NODE, NSET=FIXED
20001020, 5004.90196078431, -1170, 0
20002041, 5004.90196078431, -1167.4, 0
20003062, 5004.90196078431, -1164.8, 0
20004083, 5004.90196078431, -1162.2, 0

20457407, 5004.90196078431, -7.80000000000008, 0
20458428, 5004.90196078431, -5.20000000000013, 0
20459449, 5004.90196078431, -2.59999999999995, 0
20460470, 5004.90196078431, 0, 0
*ELEMENT, TYPE=CONN2D2, ELSET=NONREFL_EDG_X
20001020, 10001020, 20001020
20460470, 10460470, 20460470
*ELEMENT, TYPE=CONN2D2, ELSET=NONREFL_CEN_X
20002041, 10002041, 20002041
20003062, 10003062, 20003062
20004083, 10004083, 20004083
20005104, 10005104, 20005104

20456386, 10456386, 20456386
20457407, 10457407, 20457407
20458428, 10458428, 20458428
20459449, 10459449, 20459449
** DASHPOT MATERIALS
*CONNECTOR SECTION, ELSET=NONREFL_EDG_X, BEHAVIOR=DAMP_EDG_X
 CARTESIAN,
*CONNECTOR BEHAVIOR, NAME=DAMP_EDG_X
*CONNECTOR DAMPING, COMPONENT=1
679.861067725235,
*CONNECTOR DAMPING, COMPONENT=2
342.457933225413,
*CONNECTOR SECTION, ELSET=NONREFL_CEN_X, BEHAVIOR=DAMP_CEN_X
 CARTESIAN,
*CONNECTOR BEHAVIOR, NAME=DAMP_CEN_X
*CONNECTOR DAMPING, COMPONENT=1
1359.72213545047,
*CONNECTOR DAMPING, COMPONENT=2
684.915866450826,

z_Material_Section_Kinematic_JoCo2a.i

*MATERIAL,NAME=AL
*ELASTIC,TYPE=ISOTROPIC
68.9475729316836, 0.33
*DENSITY
2.71263066159991e-06,
*PLASTIC, HARDENING=COMBINED, DATA TYPE=STABILIZED
0.242161113029306, 0
0.24377685277791, 5.28489210016381e-14
0.244610116533434, 8.4558273602621e-13
0.245284632100589, 4.28076260113269e-12
0.245873108211955, 1.35293237764194e-11

0.343985014621041, 0.0524273963174091
0.344046219133387, 0.0526378421998147
0.344107399144323, 0.0528489210016381
*CYCLIC HARDENING

```
0.242161113029306, 0.0
0.242161113029306, 1.0e-9
*SOLID SECTION, ELSET=ALL, MATERIAL=AL
```

z_Sets_axi.i

```
*NSET, NSET=OUTPUTND, GENERATE
10000000, 10459450, 10210
*NSET, NSET=CENTERND, GENERATE
10000000, 10459450, 1021
*ELSET, ELSET=CENTEREL, GENERATE
10000000, 10457980, 1020
*ELSET, ELSET=OUTPUTEL0, GENERATE
10000000, 10448800, 10200
*ELSET, ELSET=OUTPUTEL
OUTPUTEL0, 10457980
```

z_Load_Time_History_var2.i

```
** Load LOAD
*Amplitude, name=LOAD_1
0, 0, 0.0075, 1.25, 0.011456751554889, 2.56218801565195, 0.015156751554889, 2.78993806148768
0.019356751554889, 2.56218801565195, 0.023556751554889, 2.24903746321123, 0.0277567515548889,
2.0040968040903, 0.0319567515548889, 1.80726877751683
0.0361567515548889, 1.64564528996719, 0.0403567515548889, 1.51055667402144, 0.0445567515548889,
1.39596402785257, 0.0487567515548889, 1.29753171155967



6.26895675155488, 0.0123072338312647, 6.27315675155488, 0.0122990080712376, 6.27735675155488,
0.0122907932995342, 6.28155675155488, 0.0122825894941512
6.28575675155488, 0.0122743966331439, 6.28995675155488, 0.0122662146946262, 6.29415675155488,
0.0122580436567704, 6.29835675155488, 0.0122498834978068
6.30255675155488, 0.0122417341960237, 6.30675675155488, 0.0122335957297671, 6.31095675155488,
0.0122254680774405, 6.31515675155488, 0.0122173512175048
```

z_BC_axi.i

```
*NSET, NSET=X_ROT, GENERATE
10001020, 10460470, 1021
*BOUNDARY
X_ROT, 4, 6, 0.0
FIXED, 1, 2, 0.0
```

z_DLOAD_G_axi_pl.i

```
10457980,P3,0.999996151354965
10457981,P3,0.999972122516612
10457982,P3,0.999924066572054



10458997,P3,3.96184224890293e-006
10458998,P3,3.86610440346851e-006
10458999,P3,3.77258940784857e-006
```

8. REFERENCES

Abaqus 2021.HF6. 2021. *The Abaqus Software is a product of Dassault Systems Similia Corp.*, Johnston, R.I.

ASME BPVC.II.D.C. 2023. *The American Society of Mechanical Engineers (ASME) Boiler and Pressure Vessel Code, Section II, Part D Properties (Customary)*. The American Society of Mechanical Engineers, Two Park Avenue, New York, NY 10016-5990.

Christman, D. R., W. M. Isbell, S. G. Babcock, A. R. McMillan, and S. J. Green. 1971. "Measurements of Dynamic Properties of Materials, Volume III, 6061-T6 Aluminum, Final Report." MSL-70-23, Vol.III, Materials and Structures Laboratory, Manufacturing Development, Genal Motors Corporation, General Motors Technical Center, Warren, MI 48090. https://apps.dtic.mil/sti/tr/pdf/AD0735966.pdf.

Fabbro, R., J. Fournier, P. Ballard, D. Devaux, and J. Virmont. 1990. "Physical study of laser-produced plasma in confined geometry." *Journal of Applied Physics* 68(2): 775 – 784. https://doi.org/10.1063/1.346783.

Grytten, F., T. Børvik, O. S. Hopperstad, and M. Langseth. 2009. "Quasi-static perforation of aa5083-h116 aluminum plates." *International Journal of Impact Engineering* 36(3): 486-497. https://doi.org/10.1016/j.ijimpeng.2008.01.015.

Johnson, G. R. and W. H. Cook. 1983. "A constitutive model and data for metals subjected to large strains, high strain rates and high temperatures." In proceedings of the 7th International Symposium on Ballistics, The Hague, The Netherlands, April 19–21, 1983.

Ocaña, J. L. et al. 2018. "The Fundamental Role of Laser-Plasma Interaction and Materials Behaviour Models in the Predictive Assessment of Residual Stresses Fields Induced in Metallic Materials by LSP." In proceedings of the 7th International Conference on Laser Peening and Related Phenomena, Singapore, June 17–22, 2018. https://oa.upm.es/55427/1/INVE_MEM_2018_296375.pdf.

Smith, J. A., J. M. Lacy, D. Lévesque, J-P. Monchalin, and M. Lord. 2016. "Use of the Hugoniot elastic limit in laser shockwave experiments to relate velocity measurements." In proceedings of the AIP Conference Proceedings, 1706(1): 080005. https://doi.org/10.1063/1.4940537.

Page intentionally left blank

Appendix A

Supplemental Information

The following was taken from “Laser Shock System, Assessing bond strength in layered materials” (https://inl.gov/wp-content/uploads/2022/10/Laser-Shock-System_1.pdf):

Laser Shock System

Assessing bond strength in layered materials

Operator using the Laser Shock System

Several industries, like nuclear, aerospace and electronic, use materials made of layered structures in their systems and components. Knowing the strength between each of these layers is essential to ensure predictable and reliable mechanical behavior of complex structures, such as nuclear fuel plates.

The Laser Shock System, developed by the U.S. High Performance Research Reactors (USHPRR) Program, can assess the fabricated interface strength of layered or composite structures and determine the debond stress thresholds from a production process. The laser shock technique was originally developed to determine how a production process affects interface strength in nuclear fuel plates; however, this testing system can be applied to different materials.

The Laser Shock System can also be used to characterize material properties such as hardness, elasticity and shear ratio. These laser-based, noncontact measurements mean that the Laser Shock System can be used in harsh process environments like those that have high temperature, radiation and corrosive conditions.

THE TECHNIQUE

The Laser Shock System creates a high-amplitude shockwave on the frontside of the layered structure via a high-energy pulsed laser.

The shock wave is monitored on the back surface as it travels through the layered structure, and the back surface velocity is used to characterize the interface. The resulting shockwave impacts the front surface, propagates as a compression wave through the structure to the unconstrained back surface, and then reflects backward through the material as a tensile wave (Figure 1).

If the reflected tensile wave exceeds the interface threshold stress, then an interior separation between

Figure 1. *Schematic of a layered structure and the Laser Shock System generating a compressional shockwave, which is converted to a backpropagating tensional shockwave.*

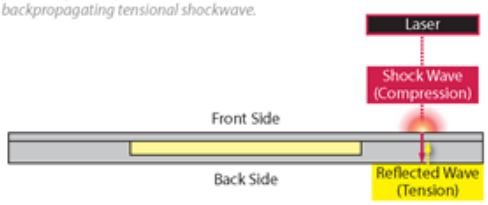

Idaho National Laboratory

Table 1. Additional material properties available from the Laser Shock System

Material Property	Measured Parameter
Hardness/temper	Hugoniot elastic limit
Elastic modulus	Primary wave velocity
Shear modulus	Shear wave speed
Residual stress	Difference between shear horizontal & vertical speeds
Material damping	Ultrasonic attenuation
Grain size and microstructure	Backscatter and frequency dispersion

layers of material occurs. Monitoring the surface velocity on the back surface of the specimen measures the energy making it to the back surface of the structure.

CAPABILITIES

- Provides localized measurements for bond strength mapping or imaging
- Identifies interface strength variations throughout a structure
- Measures debonding threshold in terms of tensile stress
- Assesses the effects from processes and process changes on the bond strength
- Determines high- and low-performance product locations within the process
- Highlights process variations within product and between products
- Uses excess material from product to predict bond strength of the product as well as detect fabrication issues

The Laser Shock System can provide additional material characterization measurements as listed in Table 1 and shown in Figure 2.

Figure 2. Laser Shock System can determine material hardness via the Hugoniot elastic limit (HEL) and measure the maximum peak velocity of the shockwave energy at the backside of the layered structure

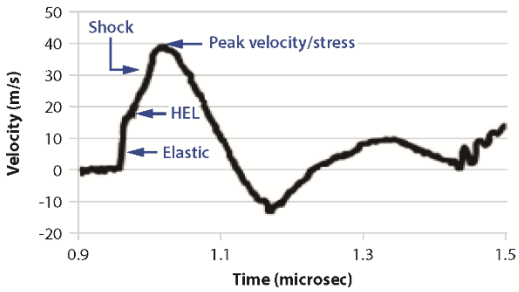

NUCLEAR APPLICATION

Nuclear fuel plates of uranium fuel foils within aluminum alloy substrates have been tested for the USHPRR Fuel Qualification Program as represented by aluminum blanks in Figure 3. The USHPRR Program endeavors to reduce proliferation risks through development of low-enriched uranium-molybdenum monolithic fuel clad in aluminum as a replacement for high-enriched uranium fuel.

In the case of nuclear fuel, weakly bonded fuel and cladding can lead to buildup of fission gases, decreasing heat transfer from the fuel. This can result in localized overheating and thermal damage and possibly fuel failure. Debonding of the cladding-cladding interface around the edge of the fuel is another possible, less-studied, failure mechanism. It can also occur from pressure buildup from fission gases or a separation failure from the plate edge propagating inward. These failure mechanisms can expose the fuel directly to reactor coolant.

These concerns must be addressed when developing new fuels and processes. The laser shock technique is the only known method to access interface integrity in producing fuel plates and can assess, in part, the suitability of the plates for insertion into the reactor.

Figure 3. Front and back of samples showing the (a) damaged transparent tape indicating the laser shock (b) outline of laser ablation, i.e., removing material with a laser, on the black tape (c) the ultrasonic raster-scan to detect interface delamination (d) plastic deformation in the aluminum

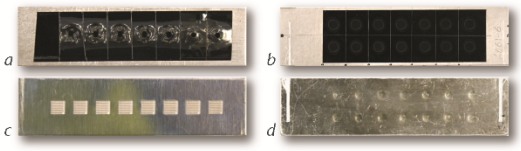

FOR MORE INFORMATION

Principal Investigator
Jim Smith
208-526-1580
james.smith@inl.gov

Lead Engineer
Brad Benefiel
208-526-7175
bradley.benefiel@inl.gov

Program Manager
Tamara Shokes
208-526-2541
tamara.shokes@inl.gov

www.inl.gov

A U.S. Department of Energy National Laboratory

22-50419_Laser_Shock_R10

Appendix B

Supplemental References for Thin Film Adhesion Strength

Here is a listing of papers that focus on FEM for modeling of interfacial stresses/adhesion strength of thin films that are bonded to elastic substrates which simulate laser shock experiments:

1. Boustie, M., E. Auroux, J-P. Romain, A. Bertoli, and D. Manesse. "Determination of the bond strength of some microns coatings using the laser shock technique." The European Physical Journal Applied Physics 5, no. 2 (1999): 149-153.

2. Grady, Martha E., Philippe H. Geubelle, and Nancy R. Sottos. "Interfacial adhesion of photodefinable polyimide films on passivated silicon." Thin Solid Films 552 (2014): 116-123.

3. Ehsani H, Boyd JD, Wang J, Grady ME. “Evolution of the Laser-Induced Spallation Technique in Film Adhesion Measurement,” Appl Mech Rev, 2021 May 1, 73(3):030802. doi:10.1115/1.4050700. Epub 2021 Apr 28. PMID: 34168374; PMCID: PMC8208493.